LASER & PHOTONICS REVIEWS
www.lpr-journal.org

Selective Generation of Luminescent Defects in Hexagonal Boron Nitride

Giacomo Venturi, Stefano Chiodini, Nicola Melchioni, Eli Janzen, James H. Edgar, Carsten Ronning, and Antonio Ambrosio**

Single photon emitters from atomic defects in crystals like hexagonal boron nitride (hBN) are vital for quantum technologies. Although various techniques are devised to obtain defects emission in hBN, simultaneous control over defects position, type, and emission spectrum has not been achieved yet. Here, ion implantation with ^{12}C, ^{20}Ne, and ^{69}Ga are used to create a composite defects population with emission ≈820 nm. The correlation of Raman and photoluminescence (PL) spectroscopy helps to identify the defects' type. After selecting Ga as the ion species yielding the maximum emitter brightness, a strategy based on thermal annealing is developed to modify the composition of the induced defects. This results in an emitter ensemble with selected spectral properties, even when starting from different implantation conditions. Specifically, thermal annealing induces a defect transmutation from one type to another, shifting the emission wavelength from 820 to 625 nm. Moreover, sample patterning is combined with focused ion beam implantation and subsequent annealing in an efficient method to deterministically set the defects position as well as the PL spectral composition. These results offer a practical avenue to achieve in situ positioning and tuning of ensembles of emitters in hBN, promising for quantum information and sensing applications.

1. Introduction

Quantum emitters, acting as sources of indistinguishable photons, are the cornerstone for developing quantum technologies.[1,2] Solid state-based emitters[3–9] are particularly attractive in terms of scalability, integrability with silicon-based technologies, cost, and the possibility of room temperature operation. Extensively studied systems include defect centers and complexes in diamond or silicon carbide,[10,11] which behave as artificial atoms emitting one photon per excitation cycle. However, two main drawbacks limit the range of applications of impurities in bulk crystals: low-temperature operation is often needed, and light extraction is limited by the high refractive index of the material.

2D materials mitigate such constraints.[3,4,12] In particular, hexagonal boron nitride (hBN)[4,13] has a large bandgap (nearly 6 eV),[14] which can accommodate defect states emitting single photons at room-temperature, with high brightness.[4]

Starting from the first evidence of single photon emitters in hBN,[4] multiple studies have reported diverse defect types, emitting photons across the visible and NIR range. Defects were found in as-grown hBN,[15,16] resulting from growth process impurities or lattice vacancies, as well as in samples after electron,[17–21] neutron[8,22] or ion beam irradiation,[17,23–29] plasma etching,[30] thermal or laser annealing,[4,17,18,31,32] and atomic force microscopy (AFM) calligraphy.[33,34] Remarkably, the ion irradiation technique can benefit, in the case of few specific ion sources (like He, Xe and, recently, Ga), from the employment of focused ion beams to reach an enhanced spatial resolution.[23,25,35]

All these methods produce three main photoluminescence (PL) signals when the material is illuminated with a sub-bandgap (in our case 532 nm) laser: emission ≈590 nm, originated from a carbon-related defect complex (whose atomic structure is still under debate)[26,27,36–38]; emission ≈625 nm, compatible with the anti-site nitrogen vacancy complex (N_BV_N), although not univocally assigned yet[4,18,23,37,39–41]; near-IR emission at 820 nm, due to a negatively charged boron vacancy (V_B^-).[24,42] These PL signals from hBN are among the brightest known from single

G. Venturi, S. Chiodini, N. Melchioni, A. Ambrosio
Centre for Nano Science and Technology
Fondazione Istituto Italiano di Tecnologia
Via Rubattino 81, Milan 20134, Italy
E-mail: giacomo.venturi@iit.it; antonio.ambrosio@iit.it

G. Venturi
Physics Department
Politecnico Milano
Piazza Leonardo Da Vinci 32, Milan 20133, Italy

E. Janzen, J. H. Edgar
Tim Taylor Department of Chemical Engineering
Kansas State University
Manhattan, KS 66506, USA

C. Ronning
Institute of Solid State Physics
Friedrich Schiller University Jena
Max-Wien-Platz 1, 07743 Jena, Germany

DOI: 10.1002/lpor.202300973

photon emitters,[43] and their yield can be further enhanced by integrating into optical cavities.[44]

In addition, similar to the nitrogen vacancy (NV) center in diamond, there is the possibility to realize a spin-photon interface with defects in hBN, thanks to their spin properties,[24,39,45] which can be exploited for quantum sensing and communication.[46]

The aforementioned techniques have been also combined with strain and external electric fields in order to possibly tune the defect emission[23,41]; however, the respective shifts obtained are small due to the slight changes of the local fields at the defect site. Large shifts or dramatic changes of the emission of defects can only be realized if the microscopic configuration of the defect changes, thus, atoms move. Up to now, there is no protocol for such a targeted manipulation of the microscopic configuration of photon emitters in hBN.

In this work, we establish a method for the deterministic generation of defects in hBN with selected spectral properties and spatial distribution. To this end, we employ ion beam irradiation to induce defects in mechanically exfoliated ^{11}B isotopically enriched hBN, whose growth technique involves very low defect concentration, which is suitable to study the effects of external generation of emitters. Ion implantation is chosen over other techniques as it involves a limited ablation of the material compared to femtosecond laser writing (where defects are located at the edges of the damaged area),[32] and it allows to change the implanted ion to explore the formation of defects involving extrinsic species, like C-related ones (which, unless the material already embeds it,[38] is not possible by electron irradiation,[18,47] for instance).

In our work, we start by comparing the outcomes of different implantations and demonstrate that Ga ions produce emitters more efficiently than the lighter carbon and neon ions. In addition, we show that Raman spectroscopy helps to identify the nature of the emitting defects upon inspection of the specific defect's vibrational properties, which is relevant for distinguishing among different emitter types. We confirm that the intensity of a specific PL peak can be correlated to the intensity of (additional) Raman peaks found only in implanted samples and associated to the specific vibrational excitation of V_B- defects in the crystal. Such correlation is observed regardless of the specific ion species used for the implantation.

Next, we demonstrate that a dramatic spectral tuning (by >200 nm) of hBN emitters can be obtained when thermal annealing is performed on implanted samples. This result is not affected if the ion species, energy, or density are varied, proving the universality of this approach. Considering this, we ascribe the concurrent changes in the PL emission to a variation of the microscopic configuration of the defects, which, once again, we confirm through Raman spectroscopy. Finally, using Ga ions in particular, we combine a commercial focused ion beam (FIB) system,[12,23,48,49] to achieve micrometric spatial resolution over a large sample area (>100 μm in lateral size), with thermal annealing to realize the unprecedented simultaneous control over the spectral properties and the spatial distribution of emitter ensembles in hBN.

2. Results and Discussion

The first practical issue in controlling single photon emitters in hBN may result from the crystal growth itself. Lattice defects of unknown type and density are in fact usually incorporated in the crystal, such as vacancies or impurity substitutions.[50] This is detrimental if the aim is to induce defects in a controlled way. For this reason, we have chosen to use high purity hBN (^{11}B isotopically enriched hBN crystals) samples, grown using metal solvents at atmospheric pressure (see Methods),[51–53] mechanically exfoliated in flakes of different thicknesses (20–150 nm) on Si substrates. The low concentration of light-emitting defects in our pristine material is confirmed by the PL measurements shown in Section S1 (Supporting Information). This sets a reference for the systematic investigation of the effect of ion irradiation in our experiment. Furthermore, starting from a pure pristine material is important in view of patterning the defects' location, that is, to achieve the best contrast with respect to non-implanted regions on the same flake.

2.1. Defects Generation with Uniform Ion Implantation

As a first step, the samples were uniformly implanted with either 13 keV $^{12}C^+$, 35 keV $^{20}Ne^+$, or 110 keV $^{69}Ga^+$ ions at an ion fluence of 1×10^{15} cm^{-2}, as sketched in **Figure 1a**. Different ion energies set the depth of the maximum ion deploying region in the sample. The energies reported above were selected to center the ion range (the center of the implanted ion distribution along the flake thickness) to the middle of specific reference flakes: 80 nm-thick for C implantation, 136 nm-thick for Ne implantation, and 146 nm-thick for Ga implantation (see Sections S2 and S3, Supporting Information). Note that, since Ne is a noble gas, it does not bind to the hBN lattice. The Ne^+ implantation is then expected to promote only the formation of defects involving intrinsic atomic species.

Figure 1b shows the respective PL spectra of the target flakes measured by illuminating with a 532 nm wavelength laser, at a diffraction limited spot far from the flakes' edges (see Methods). The figure also shows for comparison analogous data from a pristine crystal. Regardless of the implanted species, two main peaks can be observed in the spectra from each sample: one at 625 nm (orange box in Figure 1b) and another at 820 nm (yellow box).

Note that for the C implanted flake we also observed an additional peak below 600 nm, ≈590 nm (see Section S4, Supporting Information for more data). This is in agreement with a recent study reporting about a C-based color center produced by carbon implantation.[27]

The two observed main peaks are in line with previous works,[4,18,23,24,37,39–42] with the addition that from our PL spectra it emerges that Ga implanted flakes produced considerably higher PL signal compared to the C and Ne implanted ones. This is due to the heavier mass of gallium. Indeed, the heavier mass requires the use of a higher ion energy to reach the target depth in the sample (see Section S2, Supporting Information), which resulted into a considerable higher amount of implantation defects (Section S2, Supporting Information). At the same time, optical and AFM images (Section S5, Supporting Information) clearly show

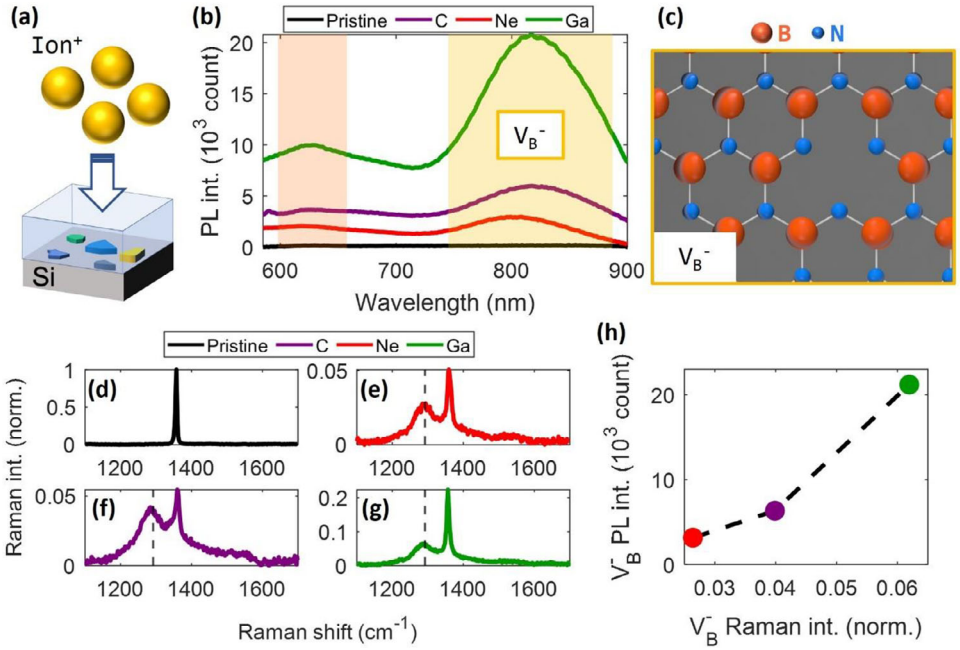

Figure 1. Uniform ion irradiation of hBN multilayer flakes on silicon. a) Illustration of the irradiation process: high energy ions (^{12}C, ^{20}Ne, and ^{69}Ga) were separately implanted in three samples hosting hBN flakes with different thicknesses (sketched by different colors). Implantation region (shaded in blue) covers homogeneously the entire surface. b) PL spectra of hBN flakes implanted with C (purple), Ne (red), and Ga (green). PL spectrum of a pristine hBN is shown in black. Main emission peaks are shaded in orange (centered at 625 nm) and yellow (centered at 820 nm). c) Schematics of the microscopic configuration of V_B^-. B and N are represented by different sizes and colors (orange and blue, respectively). d–g) Raman spectra from the hBN flakes which were also measured by PL in (b). Spectra are normalized to the pristine peak value (panel (d)) to favor a relative comparison. Line colors are chosen to match panel (b). The additional vibration mode ($\backsimeq$ 1290 cm^{-1}) in the implanted flakes is highlighted by a yellow box. h) Intensity of PL corresponding to the V_B^- peak versus intensity of Raman vibration at 1290 cm^{-1}. Each point refers to the line of the corresponding color in panels (b) and (d-g). Dashed line is just a guide for the eyes (not a data fitting).

that Ga implanted flakes were more damaged, consequence also of the concurrent sputtering during implantation.[54]

Further discussion about the induced defects' nature is supported by Raman spectroscopy, which is an often-neglected tool for studying the optical properties of hBN defects,[55] as the main target in previous works was to check the emission wavelength and the single photon purity of hBN emitters. From the Raman spectra in Figure 1d–f, we can see that next to the intrinsic hBN phonon line at 1357 cm^{-1},[56] all the implanted flakes showed a second broader peak centered at 1290 cm^{-1} (marked by the dashed line in Figure 1e–g), not present in our pristine material (Figure 1d). The appearance of this Raman peak after implantation can be interpreted as due to the vibrational properties of the induced defects, which are different from the original lattice vibrations.[57,58]

In particular, we attribute the observed feature to the presence of V_B^- (Figure 1c). In fact, recent theoretical analysis using density functional theory[57] has reported that V_B^- defects have a predicted vibrational mode ≈1300 cm^{-1}, which is in good agreement with our observation.

The fact that the peak at 1290 cm^{-1} is a Raman-active mode of V_B^- is supported by the result reported in Figure 1h, where we plot the intensity of the PL from V_B^- as a function of the intensity of the Raman peak at 1290 cm^{-1}, for each implanted sample. The positive linear trend of the data clearly shows a correlation between the V_B^- PL and its corresponding Raman peak. To better understand this graph, we stress the adopted normalization, in which the Raman peak of pristine hBN is set to one (Figure 1d). Consequently, for implanted samples, the hBN Raman signature (at 1357 cm^{-1}) peaks at a value below one, as the crystal now has many more imperfections due to the induced defects. Moreover, this value is different for each sample (Figure 1f,g), since different damage is caused by each ion specie (impinging with different energies) and because of the different thicknesses of the flakes (i.e., less material contributes to the hBN Raman peak, see Sections S2 and S3, Supporting Information). Nevertheless, this normalization does not affect the relative intensities of the observed secondary Raman peaks at 1290 cm^{-1} (Figure 1f,g) and helps in the comparison, instead. Indeed, the more V_B^- are created (higher PL signal at 820 nm), the higher the corresponding Raman-active peak. The result of Figure 1h indicates a more general relationship between the number of V_B^- and the corresponding emission at 820 nm, which is not altered by the implanted ion species. This result also emphasizes that Raman spectroscopy can be used to gain information about emitters beyond PL spectroscopy.

Finally, the absence of other peaks than the one at 1290 cm^{-1} also rules out any possible alteration of the crystal lattice toward an amorphous phase (no specific Raman features) or the transition to the cubic phase of BN (cBN)-as it might be expected when irradiating a crystal with ions. In fact, cBN is characterized by two phonon features at ≈ 1055 cm^{-1} (TO phonons) and ≈ 1305 cm^{-1} (LO phonons). The vibrational mode at 1305 cm^{-1} is usually weaker than the mode at 1055 cm^{-1} that is instead also

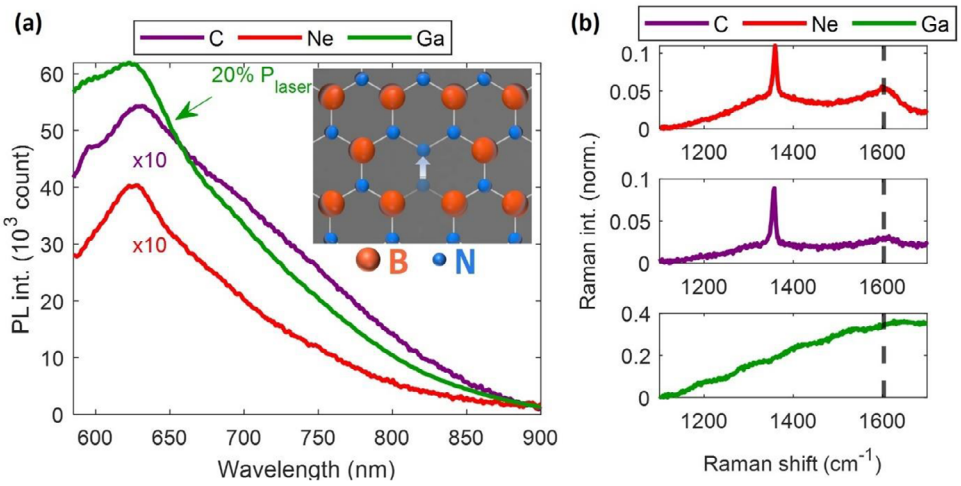

Figure 2. Thermal annealing of defects in hBN. a) PL spectra from implanted hBN after thermal annealing at 850 °C for 2 h (same flakes measured for Figure 1). PL from Ga implanted flake is collected with 20% of the laser power compared to C and Ne samples, to avoid detector saturation. PL spectrum of the C and Ne implanted flakes is magnified by a factor 10 for clarity. Inset: Sketch of the transition from V_B^- to N_BV_N defect complex. Note the only structural difference between the two: the position of the N atom. b) Raman spectra relative to the flakes of panel (a), with same normalization as in Figure 1d–g. Raman spectrum of Ga implanted flake is again collected with the same lower power as in the PL measurement. Dashed lines mark the position of the new vibration mode (≃ 1600 cm^{-1}).

IR-active.[59–61] Using scanning near-field optical microscopy we were able to locally collect mid-IR spectra on the sample (see Section S6, Supporting Information). Such spectra did not show any evidence of the IR-active mode signature of the cBN. We can thus conclude that a transition to the cubic phase during such ion implantation is negligible.

Additional PL and Raman data, collected in different conditions (i.e., for flake thicknesses differing from the one in which the ion energy was calibrated, see Section S2, Supporting Information), support our findings and can be found in Section S4 (Supporting Information).

2.2. Controlling Defect Type with Thermal Annealing

The investigation reported so far clearly shows that the majority of defects in our hBN flakes were V_B^- either after C, Ne or Ga implantation, with larger effects produced by the heavier Ga ions. This, however, with the drawback of introducing more crystal imperfections (see Section S5, Supporting Information). To relieve such damage, a practical avenue is to perform thermal annealing after implantation, an effect largely used in semiconductors industry to favor the functionalization of a semiconducting platform (such as III-V doping of silicon wafers). In our case, annealing is particularly effective on Ga implanted samples (see Section S5, Supporting Information), however, in what follows we show that thermal annealing can be used also to dramatically change the ratio between the emitters type, reducing the emission at 820 nm in favor of the emission at 625 nm.

Specifically, we studied the effect of annealing the implanted samples at 850 °C for 2 h in vacuum (10^{-4} mbar) (to prevent contamination from other atomic species, see Methods). Annealing completely changed the PL spectra of Figure 1. As shown in **Figure 2**, we observed two main differences: the peak at 820 nm reduced to almost zero; the luminescence at 625 nm increased (see Section S7, Supporting Information for more PL spectra).

The Raman spectra also changed with annealing as shown in Figure 2b. The vibration at 1290 cm^{-1} was not visible anymore, whereas a new peak at ≈1600 cm^{-1} appeared in the C and Ne implanted hBN. Such a peak is not visible in the spectrum of Ga implanted flakes, as both this additional vibration and the hBN phonon mode are buried inside the high PL signal (that is also causing a periodic modulation of the signal itself, see discussion in Section S7, Supporting Information).

The quenching with annealing of the emission at 820 nm in favor of that at 625 nm, together with the appearance of the peak at 1600 cm^{-1} and the suppression of the peak at 1290 cm^{-1}, allow us to advance the hypothesis of a specific migration of defects. According to the available literature,[47,62] as the temperature of the hBN crystal is increased, the boron vacancies become mobile (≈800 °C). Instead, nitrogen vacancies or BN divacancies require temperatures >1500 °C.[62] In such scenario, the annealing at 850 °C could provide sufficient thermal energy to the system for the mobilization of V_B^- defects, which could undergo a transition to the more stable N_BV_N configuration.[4,18,23,40,41] According to our observations then, the emission at 625 nm would be mainly due to N_BV_N, formed by transmutation of V_B^- defects over annealing. The mechanism occurring over thermal annealing is sketched in the inset of Figure 2a. A neighboring N atom of the V_B^- shifts its position into the vacancy forming an antisite and leaving an N vacancy behind, turning the V_B^- into an N_BV_N. This scenario is equivalent to the motion of the V_B^-. Note also that ref. [58] has computed a vibration frequency of 1564 cm^{-1} for the N_BV_N atomic configuration, close to the value of 1600 cm^{-1} we experimentally find in our Raman spectra.

Remarkably, the fact that the peak at 1290 cm^{-1} in the Raman spectrum disappears after annealing, together with the reduction of the PL peak of the V_B^- emission, further corroborate our

conclusion that the peaks in Figure 1e–g were due to this type of defect in the implanted samples.

Regarding the PL emission at 625 nm after annealing, its larger broadening compared to the V_B^- before the thermal treatment is evident. This fact can be tentatively explained with different reasons. On one hand, it can be traced back to the presence of different strain conditions (that are expected after ion implantation) or modifications in the dielectric environment, which are both known to shift the energy levels of hBN defects (although such tuning is not comparable to the shift obtained with annealing).[4,23,41,63] Additionally, the interaction with optical phonons may also change in these circumstances,[11] determining a smearing toward lower energies of the PL peak as a consequence of phonon emissions (i.e., a larger phonon side-band).

On the other hand, the possibility that the observed broad peak post-annealing originates from an ensemble of distinct emitter types cannot be discounted. Bearing this in mind, it is noteworthy that there is a decrease in the intensity of the Raman peak at 1600 cm^{-1} concomitant with an enhancement in the PL at 625 nm, a divergence from the pre-annealing behavior observed for the V_B^- (refer to Figure 1h). This lack of a positive correlation may be attributable to the emergence of alternative defect types (as discussed in the introduction),[27] each characterized by vibrational modes that may either be Raman-active or Raman-inactive.[58]

Even if it is not possible to clearly identify a single family of defects after the annealing, Raman spectra give meaningful insights also on the condition of the overall crystal structure. Indeed, a closer comparison between the spectra of Figures 1e,f and 2b (normalized to the same value) reveals that the Raman peak of hBN (1357 cm^{-1}) increases after annealing, pointing toward a partial restoration of the crystal structure. Indeed, the intensity of the peaks for both C- and Ne- implanted flakes double after the thermal process, increasing from 5% to 10% of the pristine value (as discussed above, no information can be deduced from the Ga implanted hBN of Figure 2b because of the strong PL covering the Raman emission). This effect, expected because of the annealing procedure, is not detectable solely from the PL emission.

Another observation about the spectra of Figure 2a is that the signal ≈625 nm is higher after annealing than before annealing (see also additional data in Section S7, Supporting Information). Comparing spectra of Figure 1b with those of Figure 2a, the enhancement in the signals (at 625 nm) for C, Ne, and Ga implanted samples is up to 20 times. Such an increase in the signal cannot be justified only by considering the conversion of one defect type into another during annealing. In this case, the overall number of defects should be almost constant, with a much lower PL enhancement after annealing. A possibility is that, on top of the defect transmutation, also the quantum efficiency of the emitters changed during the annealing, as suggested by other studies.[47] This is in line with our observation in Section S1 (Supporting Information), where we show that annealing of a pristine flake can activate defects whose emission is also ≈625 nm, although their brightness is not comparable to what is obtained with our combined process of implantation followed by annealing.

Note that, although the hypothesis of defects transmutation over annealing is reasonable and is supported by both our data (see also Section S8, Supporting Information) and the available literature,[4,18,23,40,41] the precise nature of the defects emitting at 625 nm is still debated and out of the scope of the present manuscript. Our study is rather focused on the possibility of inducing defective areas and setting their main spectral features by means of thermal annealing.

The process that we presented here-of implantation first, followed by thermal annealing at 850 °C-clearly shows the possibility of generating V_B^- emitters and then shift the emission toward spectral features 200 nm apart and with enhanced PL.

Such conclusions are not dependent upon the specific ion species (as shown in Figure 2a), which confirms the generality of the observed phenomena.

2.3. Defects Patterning with Gallium-Based FIB

The motivation for Ga implantation is not limited to our finding of its high efficiency in creating emitting centers in hBN. We investigated Ga implantation also for the possibility of implementing it in commercially available focused ion beam (FIB) systems. This is crucial in view of combining local patterning with thermal tuning of emitters to reach a unique control over defects' emission in hBN.

In this last part, we show that FIB implantation is a solid technique to achieve this goal. Note that while we were preparing this paper, it was brought to our attention that another group reported the Ga implantation with FIB. This work is summarized in ref. [29] and mostly focus on the optimization of the implantation parameters.

As sketched in **Figure 3a**, we first employed a FIB to create a pattern of 10 × 10 μm^2 areas using a 30 keV Ga ion gun with increasing ion fluences from 1.9×10^{13} to 5.7×10^{15} cm^{-2} on a pristine hBN flake (110 nm-thick; see Section S9, Supporting Information). The effect of the irradiation is immediately clear in the optical image of Figure 3b, where the implanted areas show an increasingly different contrast with respect to the surrounding pristine areas. We attribute this contrast shift to a change in the crystal refractive index caused by the increasing irradiation fluence. Concurrently, as a consequence of the damage, also the topography of the sample slightly changes (with thickness variations on the order of few nm),[54] adding a contribution to the observed contrast.

As shown in Figure 3c, the PL spectra collected at the center of each region exhibit emission at both 820 and 625 nm, in accordance with the results for the uniform irradiation (see Figure 1b). The latter increases with the ion fluence until reaching a plateau for 5.8×10^{14} cm^{-2} (region 4). A similar behavior is further observed for the (higher) PL peak at 820 nm, which peaks at a close fluence value (5.6×10^{13} cm^{-2}, region 2) and then decreases. This saturation behavior, also reported in ref. [29], can be tentatively explained considering that, when irradiating with ions, both radiative and non-radiative decay channels are induced in the crystal in the form of defects of different nature.[47] Upon changing the ion fluence, it is likely that the number of induced non-radiative decay channels grows at a different rate than the radiative centers, eventually quenching the PL emission observed in areas irradiated with high fluence.

We then performed the same annealing procedure we developed in Section 2.2 to check if it is possible to modify the spectral properties of the induced emitters while preserving the achieved

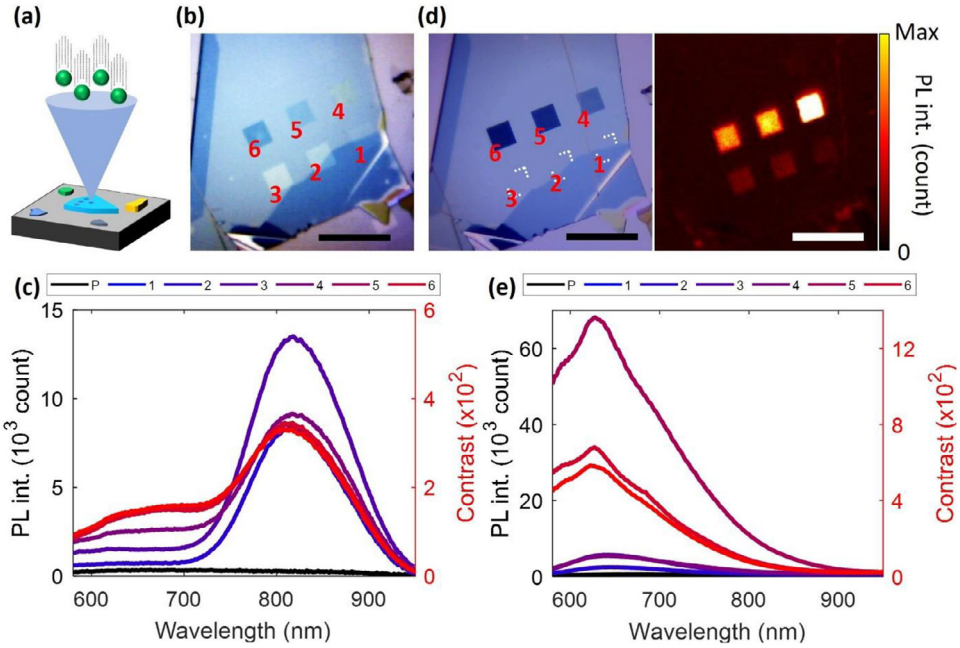

Figure 3. Spatially and spectrally controlled generation of defects in hBN using FIB. a) Sketch of FIB implantation process using Ga ions (green) with E_{ion} = 30 keV. b,d) Images of a 110 nm-thick flake. Optical image after FIB irradiation (b) and after annealing (d, left). Confocal PL map of the same flake after annealing is also shown (d, right), for identical orientation and position of the flake. The six irradiated areas are labeled in red, and the different contrast of implanted areas arises from different applied ion fluences from 1.9×10^{13} to 5.7×10^{15} cm^{-2}. c,e) PL spectra taken at the implanted areas after irradiation and after subsequent annealing, respectively. Different colors indicate implanted areas 1 to 6 (black line refers to the non-implanted area). The labels on the right y-axes refer to the signal ratio of the implanted regions with respect to the not implanted area. Black scale bars: 20 µm.

spatial resolution. The optical image reported in the left panel of Figure 3d confirms that the quality of the pattern is not hindered by the annealing. Conversely, the annealing modifies the contrast of the irradiated areas with respect to the pristine crystal. Again, this effect can be linked to a change in the crystal structure, with impact on the refractive index.

To validate this result also from the perspective of the defects' emission, we collect a confocal PL map as well. As shown in the right panel of Figure 3d, the emission pattern is clearly preserved (the orientation and position of the flake is the same as in the optical image to allow for a direct identification of the irradiated fields). From this image, we can also distinguish the regions implanted with lower ion fluences (regions 1 to 3), which are otherwise invisible in the corresponding optical image (see discussion below).

The PL signal collected after the annealing, reported in Figure 3e, shows that the peak at 820 nm disappears, while the peak at 625 nm is enhanced by the annealing for all fluences, in agreement with the data collected for homogeneous (non-localized) implantation (see Figure 2 and relative discussion). The broadening of this peak is also observed in this case, for which we refer to the discussion in Section 2.2.

Interestingly, we observed that thermal annealing also modifies the impact of the non-radiative decay channels toward a different and more efficient PL emission (the PL counts are ten times more after annealing, this is consistent with the results of the previous sections). Indeed, as emerges from a comparison of Figure 3c,e, the PL from the implanted regions peaks at a fluence $f = 5.6 \times 10^{13}$ cm^{-2} (region 2) before the annealing, while the maximum emission is reached for $f = 5.8 \times 10^{14}$ cm^{-2} (region 4) after annealing, pointing to a change in the radiative efficiency of the emitters. This hypothesis is in line with the fact that the crystal lattice undergoes a reconstruction that depends on the damage accumulated during the previous phase of implantation (i.e., on the ion fluence, which determines the number of impinging ions). For a deeper discussion of lattice healing as a function of the ion fluence, see Section S9 (Supporting Information), where the analysis of Raman spectra further confirms the previous statement. In the end, to the best of our knowledge, there are not many works in literature specifically addressing the contributions to the radiative or non-radiative decay,[47,64] hence a thorough analysis is required to better inspect the possible mechanisms.

The images of Figure 3b,d provide a visual proof of the contrast between the FIB implanted areas and our pristine material, which we also quantified in Figure 3c,e by the ratio of the signal counts from implanted regions (1 to 6) to the not implanted area (black lines). After the thermal annealing, the larger uniformity of the crystal structure lowers the optical images contrast (refractive index contrast). In particular, the less exposed areas are almost invisible. However, the PL contrast around the main peak (820 nm before annealing, and 625 nm afterward) is still on the same order of magnitude for all the implanted areas.

Such results clearly show the possibility of combining the deterministic selection of the emitting spectral range and with a precise location of the defective areas.

3. Conclusion

By taking advantage of a material platform with low intrinsic defect concentrations, we quantified the outcome of ion implantation with different ions, showing that their species affect the brightness of the emission. In particular, Ga ions produce more defects compared to lighter elements, but also more damage to the lattice. We then discussed the relevance of thermal annealing, not only to heal crystal damage, but more importantly to control the emitter structure, as different defects become mobile at different temperatures. This way, it is possible to switch the emission from the NIR to the visible by nearly 200 nm. This unprecedented result is not achievable with other already-reported tuning mechanisms (e.g., electric fields or strain), which can induce much lower shifts (<10 nm). We highlighted that the underlying mechanism is better captured by Raman spectroscopy, which even provides insights on the specific emitter nature. Specifically, we could link two different vibrational features to the two specific emissions obtained with ion implantation and annealing (irrespective of the ion species used to generate them).

We then studied the defect yield of Ga irradiation over preselected area in an FIB as a function of the ion fluence. We found that a maximum of the PL emission is reached around a fluence of 5.6×10^{14} cm^{-2} because of an interplay between the radiative centers and non-radiative decay channels induced by the irradiation. By performing the thermal annealing procedure, we proved that it is possible to shift the emitter spectral properties without hindering the achieved micrometric spatial resolution.

In conclusion, by combining ion implantation and thermal annealing, we developed a method to deterministically induce emitters in hBN with strong PL emission in a selected spectral region. On top of this, we applied our method to samples implanted with FIB, thus demonstrating that it is possible to create areas of selected emitters with micrometric spatial resolution and pre-drawn geometry.

In this work we mainly focused on ensembles of emitters, however the presented protocol can also be generalized to single photon emitters obtained with one of the techniques mentioned in the introduction, as the outcomes are independent of the defects' generation method. Hence, our results can enrich current research with interesting applications in future quantum technologies. For example, fine patterns of mixed emitters can foster new applications in quantum sensing, quantum information, and communications. For example, having an equally spaced array of two different emitters (spin-photon interfaces) on a 2D inert and cheap platform, could be a step forward in applications where spins or magnetic fields are to be detected on sub-micrometer scale.

4. Experimental Section

Sample Preparation: Hexagonal ^{11}BN crystals were grown via precipitation from a Fe solvent in a N_2/H_2 atmosphere using isotopically enriched (> 99%) elemental ^{11}B powder as the boron source material. As the source of nitrogen, naturally abundant gas was used, which is 99.6% ^{14}N and 0.4% ^{15}N. The pristine hBN flakes can contain stacking faults, dislocations, and point defects. Amongst C and O are the most common residual impurities.

Flakes were obtained by mechanical exfoliation from bulk crystals. First, a small piece (1-2 mm^2) of hBN crystal was placed onto an adhesive tape and exfoliated by folding and unfolding multiple (usually 10) times. The yielded flakes were then transferred to a Si substrate (*n*-type, 525 µm thick, lateral size 1 cm^2). To remove tape residuals, the samples (hBN + Si) were bathed in N-Methyl-2-pyrrolidone (NMP, >99%) at 85 °C for 2 h, and then rinsed with fresh NMP, acetone, and isopropyl alcohol. Finally, samples were dried with nitrogen flow.

Atomic Force Microscopy (AFM): AFM measurements were carried out at room-temperature (RH ∼ 40 %) using a Multimode 8 (Bruker) AFM microscope, with ASYELEC.01-R2 (Asylum Research, k ∼ 2.8 N·m^{-1}, ν ∼ 75 kHz) cantilevers. Measurements were performed with 0.3–0.8 Hz scan rate, with high rates for larger scans. Images were recorded when the tip-sample interaction was tuned to the repulsive regime, to avoid artifacts in retrieving sample thickness.[65] AFM images were post-processed with Gwyddion.[66]

Ion Implantation: Uniform and homogeneous ion implantation (Figures 1 and 2) of full samples (hBN on Si substrate) was done using a conventional ion implanter (High Voltage Eng.). $^{12}C^+$, $^{20}Ne^+$, and $^{69}Ga^+$ ions were accelerated to ion energies between 13 and 110 keV and implanted with different ion fluences.

Focused ion beam (FIB) irradiation was performed with a Helios NanoLab 600i FEI system. This technique was used to finely structure the hBN flakes (Figure 3), thanks to a nominal beam diameter of 7 nm. The employed beam current is 1.1 pA.

For both the uniform and FIB irradiations, an incidence angle of 7° (see Figure S1, Supporting Information) was chosen to avoid channeling, that is, the unperturbed transit of ions in the crystal taking place along high symmetry directions. All the implantations were done at room temperature, and the corresponding damage and ion range profiles were simulated using the software package TRIM/SRIM.[67]

Thermal Annealing: Thermal annealing was performed using a rapid thermal annealer UniTemp RTP-150-HV to heat the samples at 850 °C in high vacuum (10^{-4} mbar) for 2 h. Nitrogen flow was employed to cool the samples at the end of the process. The effects of a different annealing temperature (1000 °C) on pristine flakes were also explored, as reported in Section S1 (Supporting Information).

Photoluminescence (PL) and Raman Spectroscopy: PL and Raman measurements (on a single, diffraction limited, point of the sample, i.e., point spectroscopy) were performed with a commercial inVia Raman microscope (Renishaw) coupled to a 532 nm diode laser (power on sample plane of ≈500 µW), which was focused through a 50× objective (NA = 0.75). All the measurements were done in air at room-temperature.

PL measurements simply consist of extended Raman measurements (hence with the same spectral resolution). Specifically, the collection grating was rotated at discrete steps to steer different wavelengths on a calibrated CCD. A Raman spectrum was collected for each orientation of the grating, and a wider spectrum was reconstructed appending the sequential spectra at different grating positions. An integration time of 10 s was used for the measurements. The spectrometer was calibrated to the 520 cm^{-1} line of silicon. A grating with 1800 lines/mm was employed, hence with a spectral resolution below 2 cm^{-1} in the 532–1000 nm range.

PL measurements were always performed far from the edges of the flakes and on flat regions, to avoid influences from fabrication-induced defects, strain, and edge effects (like additional scattering). A gaussian moving average with a 2 nm window was performed on the PL data to reduce noise (but not on the Raman spectra), without affecting the interpretation of the results, as witnessed by the comparison with raw data reported in Section S10 (Supporting Information).

Confocal PL maps were collected with a home-built setup based on a Nikon inverted microscope (same objective used for point spectroscopy) coupled with a 532 nm laser.

Mid-IR nanospectroscopy: Nano-Fourier transform infrared (nano-FTIR) spectroscopy was performed by focusing a broadband laser under an oscillating AFM tip close to the sample and detecting the reflected light. The setup was a commercial asymmetric Michelson interferometer, where one of the arms hosts the tip-sample system (NeaSpec), coupled to a mid-IR source, whose spectrum was generated by superimposing two near-IR

fiber coupled lasers (FemtoFiber pro IR and SCIR, Toptica) on a GeSe crystal for difference frequency generation. The output was tunable from 700 to 2500 cm^{-1} (with a bandwidth of roughly 800 cm^{-1}) by the orientation of the crystal, with a total output power of ≈1 mW.

Demodulation of the tip-sample scattered signal with a lock-in set at $n = 1, 2, 3, \ldots$ times the frequency of the AFM tip was performed to select the near-field signal coming from the pure tip-sample interaction (hence, reaching a spatial resolution compared to the tip radius, ≈50 nm).

Due to the geometry of the interferometer, it is possible to retrieve both the amplitude and phase of the scattered near-field ($E_n = a_n e^{i\varphi_n}$, where a_n and φ_n are the amplitude and phase at demodulation order n, respectively).

All the experiments were carried out in air and at room temperature.

Supporting Information

Supporting Information is available from the Wiley Online Library or from the author.

Acknowledgements

The authorss thank Oliver Rüger and Patrick Hoffmann for performing the ion irradiations. The authors would like to thank Gabriele Grosso for fruitful discussions about the results. Rhe authors also acknowledge funding from ERC grants "METAmorphoses", grant agreement no. 817794, Fondazione Cariplo, grant no 2019–3923 and the Deutsche Forschungsgemeinschaft within the CRC 1375 "NOA" (project B5). The Office of Naval Research supported the hBN crystal growth through award N00014-22-1-2582.

Conflict of Interest

The authors declare no conflict of interest.

Data Availability Statement

The data that support the findings of this study are available from the corresponding author upon reasonable request.

Keywords

defects, hexagonal boron nitride, ion implantation, quantum technologies, single photon emitters

Received: September 29, 2023
Revised: January 7, 2024
Published online: February 11, 2024

[1] B. Lounis, M. Orrit, *Rep. Prog. Phys.* **2005**, *68*, 1129.
[2] M. Ruf, N. H. Wan, H. Choi, D. Englund, R. Hanson, *J. Appl. Phys.* **2021**, *130*, 070901.
[3] M. Koperski, K. Nogajewski, A. Arora, V. Cherkez, P. Mallet, J.-Y. Veuillen, J. Marcus, P. Kossacki, M. Potemski, *Nat. Nanotechnol.* **2015**, *10*, 503.
[4] T. T. Tran, K. Bray, M. J. Ford, M. Toth, I. Aharonovich, *Nat. Nanotechnol.* **2016**, *11*, 37.
[5] I. Aharonovich, D. Englund, M. Toth, *Nat. Photonics* **2016**, *10*, 631.
[6] C. Palacios-Berraquero, D. M. Kara, A. R.-P. Montblanch, M. Barbone, P. Latawiec, D. Yoon, A. K. Ott, M. Loncar, A. C. Ferrari, M. Atatüre, *Nat. Commun.* **2017**, *8*, 15093.
[7] J. Lee, V. Leong, D. Kalashnikov, J. Dai, A. Gandhi, L. A. Krivitsky, *AVS Quantum Sci.* **2020**, *2*, 031701.
[8] J. Li, E. R. Glaser, C. Elias, G. Ye, D. Evans, L. Xue, S. Liu, G. Cassabois, B. Gil, P. Valvin, *Chem. Mater.* **2021**, *33*, 9231.
[9] T. Gao, M. von Helversen, C. Anton-Solanas, C. Schneider, T. Heindel, *npj 2D Mater. Appl.* **2023**, *7*, 4.
[10] I. Aharonovich, S. Castelletto, D. Simpson, C.-H. Su, A. Greentree, S. Prawer, *Rep. Prog. Phys.* **2011**, *74*, 076501.
[11] F. Fuchs, B. Stender, M. Trupke, D. Simin, J. Pflaum, V. Dyakonov, G. Astakhov, *Nat. Commun.* **2015**, *6*, 7578.
[12] M. Kianinia, Z.-Q. Xu, M. Toth, I. Aharonovich, *Appl. Phys. Rev.* **2022**, *9*, 011306.
[13] J. D. Caldwell, I. Aharonovich, G. Cassabois, J. H. Edgar, B. Gil, D. Basov, *Nat. Rev. Mater.* **2019**, *4*, 552.
[14] G. Cassabois, P. Valvin, B. Gil, *Nat. Photonics* **2016**, *10*, 262.
[15] T. T. Tran, C. Zachreson, A. M. Berhane, K. Bray, R. G. Sandstrom, L. H. Li, T. Taniguchi, K. Watanabe, I. Aharonovich, M. Toth, *Phys. Rev. Appl.* **2016**, *5*, 034005.
[16] N. Mendelson, Z.-Q. Xu, T. T. Tran, M. Kianinia, J. Scott, C. Bradac, I. Aharonovich, M. Toth, *ACS Nano* **2019**, *13*, 3132.
[17] S. Choi, T. T. Tran, C. Elbadawi, C. Lobo, X. Wang, S. Juodkazis, G. Seniutinas, M. Toth, I. Aharonovich, *ACS Appl. Mater. Interfaces* **2016**, *8*, 29642.
[18] T. T. Tran, C. Elbadawi, D. Totonjian, C. J. Lobo, G. Grosso, H. Moon, D. R. Englund, M. J. Ford, I. Aharonovich, M. Toth, *ACS Nano* **2016**, *10*, 7331.
[19] C. Fournier, A. Plaud, S. Roux, A. Pierret, M. Rosticher, K. Watanabe, T. Taniguchi, S. Buil, X. Quélin, J. Barjon, *Nat. Commun.* **2021**, *12*, 3779.
[20] A. Gale, C. Li, Y. Chen, K. Watanabe, T. Taniguchi, I. Aharonovich, M. Toth, *ACS Photonics* **2022**, *9*, 2170.
[21] A. Kumar, C. Cholsuk, A. Zand, M. N. Mishuk, T. Matthes, F. Eilenberger, S. Suwanna, T. Vogl, *APL Mater.* **2023**, *11*, 071108.
[22] A. Gottscholl, M. Diez, V. Soltamov, C. Kasper, D. Krauße, A. Sperlich, M. Kianinia, C. Bradac, I. Aharonovich, V. Dyakonov, *Nat. Commun.* **2021**, *12*, 4480.
[23] G. Grosso, H. Moon, B. Lienhard, S. Ali, D. K. Efetov, M. M. Furchi, P. Jarillo-Herrero, M. J. Ford, I. Aharonovich, D. Englund, *Nat. Commun.* **2017**, *8*, 705.
[24] A. Gottscholl, M. Kianinia, V. Soltamov, S. Orlinskii, G. Mamin, C. Bradac, C. Kasper, K. Krambrock, A. Sperlich, M. Toth, *Nat. Mater.* **2020**, *19*, 540.
[25] M. Kianinia, S. White, J. E. Fröch, C. Bradac, I. Aharonovich, *ACS Photonics* **2020**, *7*, 2147.
[26] M. Fischer, J. M. Caridad, A. Sajid, S. Ghaderzadeh, M. Ghorbani-Asl, L. Gammelgaard, P. Bøggild, K. S. Thygesen, A. V. Krasheninnikov, S. Xiao, *Sci. Adv.* **2021**, *7*, eabe7138.
[27] N. Mendelson, D. Chugh, J. R. Reimers, T. S. Cheng, A. Gottscholl, H. Long, C. J. Mellor, A. Zettl, V. Dyakonov, P. H. Beton, *Nat. Mater.* **2021**, *20*, 321.
[28] N.-J. Guo, W. Liu, Z.-P. Li, Y.-Z. Yang, S. Yu, Y. Meng, Z.-A. Wang, X.-D. Zeng, F.-F. Yan, Q. Li, *ACS Omega* **2022**, *7*, 1733.
[29] M. Hennessey, B. Whitefield, J. A. Scott, M. Kianinia, I. Aharonovich, M. Toth, **2023**, https://doi.org/10.48550/arXiv.2303.06784.
[30] Z.-Q. Xu, C. Elbadawi, T. T. Tran, M. Kianinia, X. Li, D. Liu, T. B. Hoffman, M. Nguyen, S. Kim, J. H. Edgar, *Nanoscale* **2018**, *10*, 7957.
[31] S. Hou, M. D. Birowosuto, S. Umar, M. A. Anicet, R. Y. Tay, P. Coquet, B. K. Tay, H. Wang, E. H. T. Teo, *2D Mater.* **2017**, *5*, 015010.
[32] X. Gao, S. Pandey, M. Kianinia, J. Ahn, P. Ju, I. Aharonovich, N. Shivaram, T. Li, *ACS Photonics* **2021**, *8*, 994.
[33] C. Li, N. Mendelson, R. Ritika, Y. Chen, Z.-Q. Xu, M. Toth, I. Aharonovich, *Nano Lett.* **2021**, *21*, 3626.
[34] M. R. Rosenberger, C. K. Dass, H.-J. Chuang, S. V. Sivaram, K. M. McCreary, J. R. Hendrickson, B. T. Jonker, *ACS Nano* **2019**, *13*, 904.

[35] E. Glushkov, M. Macha, E. Rath, V. Navikas, N. Ronceray, C. Y. Cheon, A. Ahmed, A. Avsar, K. Watanabe, T. Taniguchi, *ACS Nano* **2022**, *16*, 3695.
[36] A. Sajid, K. S. Thygesen, *2D Mater.* **2020**, *7*, 031007.
[37] I. Aharonovich, J.-P. Tetienne, M. Toth, *Nano Lett.* **2022**, *22*, 9227.
[38] M. Neumann, X. Wei, L. Morales-Inostroza, S. Song, S.-G. Lee, K. Watanabe, T. Taniguchi, S. Götzinger, Y. H. Lee, *ACS Nano* **2023**, *17*, 11679.
[39] H. L. Stern, Q. Gu, J. Jarman, S. E. Barker, N. Mendelson, D. Chugh, S. Schott, H. H. Tan, H. Sirringhaus, I. Aharonovich, *Nat. Commun.* **2022**, *13*, 618.
[40] Y. Xue, H. Wang, Q. Tan, J. Zhang, T. Yu, K. Ding, D. Jiang, X. Dou, J.-j. Shi, B.-q. Sun, *ACS Nano* **2018**, *12*, 7127.
[41] G. Noh, D. Choi, J.-H. Kim, D.-G. Im, Y.-H. Kim, H. Seo, J. Lee, *Nano Lett.* **2018**, *18*, 4710.
[42] V. Ivády, G. Barcza, G. Thiering, S. Li, H. Hamdi, J.-P. Chou, Ö. Legeza, A. Gali, *npj Comput. Mater.* **2020**, *6*, 41.
[43] A. Bommer, C. Becher, *Nanophotonics* **2019**, *8*, 2041.
[44] N. Mendelson, R. Ritika, M. Kianinia, J. Scott, S. Kim, J. E. Fröch, C. Gazzana, M. Westerhausen, L. Xiao, S. S. Mohajerani, *Adv. Mater.* **2022**, *34*, 2106046.
[45] F. F. Murzakhanov, G. V. Mamin, S. B. Orlinskii, U. Gerstmann, W. G. Schmidt, T. Biktagirov, I. Aharonovich, A. Gottscholl, A. Sperlich, V. Dyakonov, *Nano Lett.* **2022**, *22*, 2718.
[46] A. Al-Juboori, H. Z. J. Zeng, M. A. P. Nguyen, X. Ai, A. Laucht, A. Solntsev, M. Toth, R. Malaney, I. Aharonovich, *Adv. Quantum Technol.* **2023**, *6*, 2300038.
[47] S. A. Breitweiser, A. L. Exarhos, R. N. Patel, J. Saouaf, B. Porat, D. A. Hopper, L. C. Bassett, *ACS Photonics* **2019**, *7*, 288.
[48] N. Bassim, K. Scott, L. A. Giannuzzi, *MRS Bull.* **2014**, *39*, 317.
[49] Thermo Scientific, https://assets.thermofisher.com/TFS-Assets/MSD/Datasheets/scios-2-datasheet-materials-science.pdf (accessed: July **2023**).
[50] L. Song, L. Ci, H. Lu, P. B. Sorokin, C. Jin, J. Ni, A. G. Kvashnin, D. G. Kvashnin, J. Lou, B. I. Yakobson, *Nano Lett.* **2010**, *10*, 3209.
[51] K. Chaudhary, M. Tamagnone, X. Yin, C. M. Spägele, S. L. Oscurato, J. Li, C. Persch, R. Li, N. A. Rubin, L. A. Jauregui, *Nat. Commun.* **2019**, *10*, 4487.
[52] G. Pavlidis, J. J. Schwartz, J. Matson, T. Folland, S. Liu, J. H. Edgar, J. D. Caldwell, A. Centrone, *APL Mater.* **2021**, *9*, 091109.
[53] S. Liu, R. He, L. Xue, J. Li, B. Liu, J. H. Edgar, *Chem. Mater.* **2018**, *30*, 6222.
[54] R. Klaiss, J. Ziegler, D. Miller, K. Zappitelli, K. Watanabe, T. Taniguchi, B. Alemán, *J. Chem. Phys.* **2022**, *157*.
[55] While this manuscript was under review, we became aware of recent publications that also explore the spectral analysis of defects generated in hexagonal boron nitride (hBN) using focused ion beam (FIB) techniques. These publications, Guan-Lin Liu et al. (*Adv. Opt. Mater.* **2023**, https://doi.org/10.1002/adom.202302083) and Soumya Sarkar et al. (*Nanolett.* **2024**, *24*, 43), were not considered in the preparation of our manuscript but are relevant to the context of this study.
[56] T. Vuong, S. Liu, A. Van der Lee, R. Cuscó, L. Artús, T. Michel, P. Valvin, J. Edgar, G. Cassabois, B. Gil, *Nat. Mater.* **2018**, *17*, 152.
[57] C. Linderälv, W. Wieczorek, P. Erhart, *Phys. Rev. B* **2021**, *103*, 115421.
[58] S. A. Tawfik, S. Ali, M. Fronzi, M. Kianinia, T. T. Tran, C. Stampfl, I. Aharonovich, M. Toth, M. J. Ford, *Nanoscale* **2017**, *9*, 13575.
[59] S. Reich, A. Ferrari, R. Arenal, A. Loiseau, I. Bello, J. Robertson, *Phys. Rev. B* **2005**, *71*, 205201.
[60] H. Hofsäss, C. Ronning, U. Griesmeier, M. Gross, S. Reinke, M. Kuhr, *Appl. Phys. Lett.* **1995**, *67*, 46.
[61] M. Eremets, M. Gauthier, A. Polian, J. Chervin, J. Besson, G. Dubitskii, Y. Y. Semenova, *Phys. Rev. B* **1995**, *52*, 8854.
[62] A. Zobelli, C. Ewels, A. Gloter, G. Seifert, *Phys. Rev. B* **2007**, *75*, 094104.
[63] S. Li, J.-P. Chou, A. Hu, M. B. Plenio, P. Udvarhelyi, G. Thiering, M. Abdi, A. Gali, *npj Quantum Inform.* **2020**, *6*, 85.
[64] S. X. Li, T. Ichihara, H. Park, G. He, D. Kozawa, Y. Wen, V. B. Koman, Y. Zeng, M. Kuehne, Z. Yuan, *Commun. Mater.* **2023**, *4*, 19.
[65] P. Nemes-Incze, Z. Osváth, K. Kamarás, L. Biró, *Carbon* **2008**, *46*, 1435.
[66] Gwyddion, http://gwyddion.net/ (accessed: June **2023**).
[67] SRIM, http://www.srim.org/ (accessed: June **2023**).